ACS APPLIED MATERIALS & INTERFACES

Research Article

www.acsami.org

Local Modification of the Microstructure and Electrical Properties of Multifunctional Au−YSZ Nanocomposite Thin Films by Laser Interference Patterning

Thomas Gries,[†,‡] Rodolphe Catrin,[†] Sylvie Migot,[‡] Flavio Soldera,[†] Jose-Luis Endrino,[§] Angel R. Landa-Canovas,[∥] Franck Cleymand,[‡] Denis Mangin,[‡] Frank Mücklich,[†] and David Horwat*[,‡]

[†]Department of Materials Science and Engineering, Chair of Functional Materials, Saarland University, Campus D3.3, D-66123 Saarbrücken, Germany

[‡]Institut Jean Lamour, UMR7198, Université de Lorraine, F-54011 Nancy, France

[§]Department of Manufacturing and Materials, Cranfield University, MK43 0AL Bedfordshire, United Kingdom

[∥]Instituto de Ciencia de Materiales de Madrid (ICMM), Consejo Superior de Investigaciones Cientificas (CSIC), Cantoblanco, E-28049 Madrid, Spain

Supporting Information

ABSTRACT: Nanocomposite films consisting of gold nanoparticles embedded in an yttria-stabilized zirconia matrix (Au−YSZ) have been synthesized with different gold loadings by reactive magnetron sputtering followed by ex situ annealing in air or laser interference patterning (LIP) treatment. It is shown that the electrical conductivity of the nanocomposite films can be modified to a large extent by changing the gold loading, by thermal annealing, or by LIP. The structural and microstructural analyses evidenced the segregation of metallic gold in crystalline form for all synthesis conditions and treatments applied. Thermal annealing above 400 °C is observed to trigger the growth of pre-existing nanoparticles in the volume of the films. Moreover, pronounced segregation of gold to the film surface is observed for Au/(Au + Zr + Y) ratios above 0.40, which may prevent the use of thermal annealing to functionalize gold-rich Au−YSZ coatings. In contrast, significant modifications of the microstructure were detected within the interference spot (spot size close to 2 × 2 mm) of LIP treatments only for the regions corresponding to constructive interference. As a consequence, besides its already demonstrated ability to modify the friction behavior of Au−YSZ films, the LIP treatment enables local tailoring of their electrical resistivity. The combination of these characteristics can be of great interest for sliding electrical contacts.

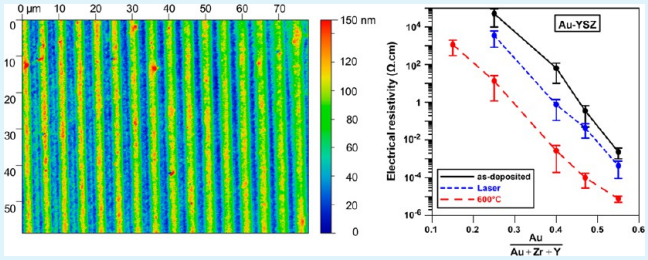

KEYWORDS: *nanocomposite films, electrical conductivity, gold nanoparticles, laser interference patterning, thermal annealing, microstructure*

1. INTRODUCTION

The gold/yttria-stabilized zirconia (Au−YSZ) nanocomposite system is a particularly interesting candidate for multifunctional applications. First, oxide-supported gold nanoparticles are very promising to dramatically lower the inset temperature of several catalytic reactions to room temperature or close to room temperature.[1] This approach currently stimulates many studies in the field of heterogeneous catalysis. Second, gold nanoparticles on different supports and gold/oxide nanocomposite films exhibit localized surface plasmon resonance (LSPR) in the visible range, making it useful for applications as a chemical sensing layer[2,3] and in the emerging field of plasmonics. Effectively, it enables combining the specific properties of YSZ, such as oxide ion conductivity, to the LSPR and catalytic activity provided by the gold nanoparticles. Third, as long as the gold loading is sufficient, annealing such films in air induces the relocation at the surface of some of the gold atoms to form a soft layer with adaptive tribological properties.[4]

The principle of the so-called laser interference patterning (LIP)[5] is based on the interference of two beams of light from a high-energy nanosecond pulse laser source on the surface of the material. The interaction of the beams with the material leads to a periodic thermal treatment with local heating of the surface in a well-defined geometrical pattern. Due to a high local thermal gradient produced in a very short time, this one-step process produces metallurgical effects such as lateral grain growth,[6,7] chemical decomposition,[8] intermetallic phase precipitation,[9] and surface segregation.[10] We showed recently that the LIP method locally triggers the relocation of gold atoms in

Received: May 21, 2014
Accepted: July 24, 2014
Published: July 24, 2014

the regions of interference maxima and generates periodic topography that limits the contact surface between reciprocate sliding surfaces.[10] We believe this is of interest for adjusting the local tribological characteristics of multifunctional optically/catalytically active materials or microsystems subject to localized mechanical requirements.

In addition to the explored properties of Au−YSZ films mentioned above, the metallic conductivity of gold can be used to reduce the electrical resistance in Au−YSZ thin films, which is not considered in the literature. The present study aims at spreading the idea that such films can be used as multifunctional layers by studying the effects of gold loading, thermal annealing, and LIP on the morphology, microstructure, and electrical properties of Au−YSZ nanocomposite films synthesized by reactive magnetron cosputtering.

2. EXPERIMENTAL SECTION

2.1. Film Deposition. Thin films of the Zr−Y−Au−O system were deposited on soda lime glass slides and silicon substrates by reactive magnetron cosputtering of Au and $Zr_{0.84}Y_{0.16}$ targets (50 mm diameter, 3 mm thick, and purity greater than 99.9%) in an Ar−O_2 reactive gas mixture. A base vacuum of about 10^{-4} Pa was ensured in the deposition chamber by a mechanical pump and a diffusion oil pump. The experimental device was equipped with two unbalanced magnetron systems separated 100 mm from each other, placed symmetrically relative to the rotating substrate-holder axis. The distance between the substrates and the Au and $Zr_{0.84}Y_{0.16}$ targets was fixed to 100 and 50 mm, respectively. The substrates were cleaned using ethanol and by Ar^+ ion impingement using a 100 W radio frequency glow discharge for 1 min just before deposition. The $Zr_{0.84}Y_{0.16}$ target was powered by a pulsed DC Advanced Energy Pinnacle +5 kW generator operated at a frequency of 50 kHz with an off-time of 4 μs. The current applied to the target was fixed at 0.7 A. The Au target was powered by a DC Advanced Energy MDX 1.5 kW generator, and the current was varied in the 0−0.1 A range (Table 1).

Table 1. Deposition Conditions, Thickness, and Composition of Au−YSZ Thin Films Synthesized by Reactive Magnetron Cosputtering of Au and $Zr_{0.84}Y_{0.16}$ Targets

sample	thickness (nm)	deposition time (min:s)	current metal target (A)	Au/(Zr + Y + Au)
YSZ	300	20:00	0	0
15% Au−YSZ	200	10:00	0.02	0.15
25% Au−YSZ	120	8:30	0.03	0.25
40% Au−YSZ	150	8:00	0.05	0.40
47% Au−YSZ	120	5:30	0.07	0.47
55% Au−YSZ	100	3:45	0.1	0.55

Argon and oxygen flow rates were fixed at 20 and 6.3 sccm, respectively, leading to a total pressure close to 0.25 Pa. It was verified that such conditions led to the complete oxidation of zirconium and yttrium atoms in cubic yttria-stabilized zirconia when the $Zr_{0.84}Y_{0.16}$ target was sputtered alone. The films were deposited without external heating, which enabled us to maintain the deposition temperature below 50 °C. As-deposited films, LIP treated films, and films annealed in air for 2 h using a conventional furnace equipped with a thermocouple were investigated for their structural and electrical properties.

2.2. Laser Interference Patterning. The laser interference patterning process was performed using a high-power nanosecond pulsed Nd:YAG laser (Spectra Physics, Quanta Ray PRO 290) with a fundamental wavelength of 1064 nm, a repetition rate of 10 Hz, and a pulse duration of 10 ns. The laser beam has an almost Gaussian intensity distribution in space and time. The third harmonic (355 nm) was used according to the good absorbance of the metals at this wavelength. The primary laser beam was split into two coherent beams that were recombined on the sample surface to create line-pattern interferences (Figure 1). A treated area of 18 × 18 mm was

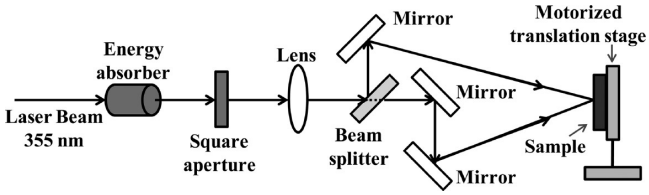

Figure 1. Schematic setup of the laser interference system. The primary laser beam is divided into two sub-beams, which are focused to interfere on the sample surface.

constructed using 2 × 2 mm spots and single pulse exposure of the material to the interfering laser beam with an energy density of 91 mJ cm^{-2}. The periodicity, P, of the interference pattern can be controlled as a function of the laser wavelength λ and the angle α between the beams. The spacing of the structures can be described by

$$P = \frac{\lambda}{2\sin(\alpha/2)}$$

Using an incident angle of 3.8°, we obtained a line-pattern structure period of 5.35 (±0.3) μm.

2.3. Sample Characterization. The determination of topographic parameters such as structure depth, periodicity, and roughness was carried out by white light interferometry (WLI) using a Zygo New View 200 interferometer equipped with a 40× Mirau interference objective.

The surface morphology was imaged with a high-resolution scanning electron microscope (SEM) FEI Helios Nanolab 600 equipped with a field emission gun and using an acceleration voltage of 5 kV. The chemical composition of the films was determined by analyzing the top of the films via an energy-dispersive spectrometer (EDS) coupled to the SEM. Due to the uncertainty on the oxygen chemical contents measured by EDS, the Au/(Au + Zr + Y) ratio of atomic concentrations was used as an indicator of the gold loading. The microscope is also equipped with a focused ion beam (FIB). Thin lamellae for transmission electron microscopy (TEM) analysis were prepared with this dual beam workstation using the lift out method. The thin foils were extracted after FIB-milling with an Omniprobe 100 micromanipulator, fixed in Cu-holder, and then further thinned for electron transparency. The thinning was done first with 30 kV accelerating voltage and then with 5 kV accelerating voltage to minimize any possible preparation artifact. The TEM analysis was carried out with a Philips CM 200 microscope to provide further details on the microstructures of selected samples. High-resolution transmission electron microscopy (HRTEM) and scanning TEM-electron energy-loss spectroscopy (STEM-EELS) studies were carried out on a selected sample with a JEM 3000F microscope operating at 300 kV (double tilt, 20°; point resolution, 1.7 Å), fitted with an ENFINA 1000 spectrometer and a JEOL annular dark-field (ADF) detector. The STEM images were acquired with a collection angle of ∼30 mrad. The spectral maps were acquired in STEM mode, with an electron probe size diameter of ∼1 nm, a collection time of 2 s, a dispersion of 0.5 eV/pixel, and a collection semiangle of $\beta \approx 8.9$ mrad. The background under each spectrum was subtracted following a power-law model. EELS experiments showed the presence of oxygen, but gold peaks were difficult to see. Therefore, high-angle annular dark-field (HAADF) STEM was used to obtain a mapping of gold, because in those conditions, the scattering is proportional to Z^2 and, therefore, dominated by gold. The O and Au elemental map was constructed by superimposing the EELS O−K image and the HAADF image at the same region of the sample.

Secondary ion mass spectrometry (SIMS) measurements were conducted on selected samples using SIMS CAMECA IMS7F equipment. A Cs+ primary beam of 3 kV impact energy and 20 nA current was used. To limit matrix effects, we performed elemental profile analyses by counting CsE^+ ions (where E is the element to be measured) under a mass resolution (M/dM) of 1200 at 10% peak height. The signal was collected by scanning a 150 × 150 μm area of the sample surface with an electronic gate of 70%.

The film structure was also studied by X-ray diffraction in grazing incidence geometry (GIXRD) using the Co Kα radiation (0.178897 nm) with a Bruker D8 Discover diffractometer at a 4° incidence angle. A characteristic length of coherence domains in gold nanoparticles in the composite films can be extracted from the full width at half-maximum of an fcc gold diffraction peak using the Scherrer formula after correction from the experimental broadening:[11]

$$d = \frac{0.89 \times \lambda}{\beta \times \cos \sigma}$$

where d is the length of coherence domains, λ is the X-ray wavelength, β is the full width at half-maximum of the diffraction peak, and σ is the diffraction angle.

The film thicknesses were measured using the step method by tactile profilometry and have been confirmed by SEM cross-section observations.

The electrical resistivity was deduced using the value of the film thickness and from sheet resistance measurements using the four-point probe method at room temperature (Keithley 237 current source and Keithley 2700 multimeter). This equipment enabled us to measure electrical resistivity below 1×10^5 Ω·cm.

Kelvin probe force microscopy (KPFM) measurements were conducted on a selected interfered sample. For this purpose, a Veeco diDimension atomic force microscope was used in amplitude feedback mode using an RFESP n-type silicon tip (phosphorus-doped from Brücker) exhibiting a resistivity of 1−10 Ω·cm, a fundamental resonance frequency (ν_0) of 78.7 kHz, and a stiffness constant (k) of 3 N/m. After collecting the topography of the sample on a 5 × 5 μm area with 512 × 512 pixels at 0.5 Hz, we set the tip−substrate distance to 50 nm in order to collect the contact potential difference (CPD) between the tip and sample surface at the same area and scanning conditions. We verified that the surface topography has a limited influence on the value of CPD measured. The CPD is related to the work functions of the sample θ_s and tip θ_t through the following relationship:

$$\mathrm{CPD} = \frac{\theta_s - \theta_t}{e}$$

where e is the electronic charge. Principles and some applications of the KPFM method can be found in the literature.[12]

3. RESULTS AND DISCUSSION

3.1. Structure and Microstructure. Some characteristics of the coatings deposited with the reactive cosputtering process for the different experimental parameters explored within this study are summarized in Table 1. The Au/(Au + Zr + Y) ratio can be tuned by changing the current applied to the gold target. Figure 2 represents the evolution of this ratio with the power dissipated by the Au target, P_{Au}, obtained from the discharge current applied to the target and discharge voltage read on the generator front panel. There is a monotonous, reproducible, and smooth increase of the gold content with P_{Au}. This ratio ranges from 0 to 0.55, depending on the discharge parameters. It is worth noting that the atomic ratio of zirconium to yttrium was very close to that of the $Zr_{0.84}Y_{0.16}$ target, which was shown to be sufficient to stabilize the cubic form of zirconia in bulk samples. SEM observations of the surface and cross section of the films were systematically conducted for all explored conditions. All the deposited coatings presented a smooth surface topography and a dense morphology with a thickness in the 100−200 nm range.

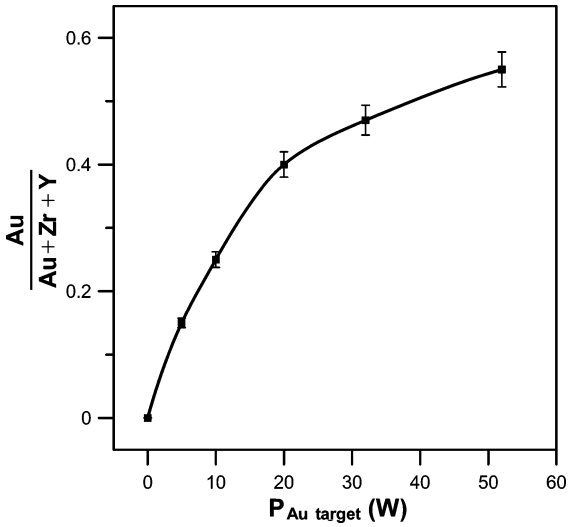

Figure 2. Evolution of the thin film composition as a function of the power applied to the gold target.

The XRD diffractograms of as-deposited films and films in situ annealed in argon at different temperatures are shown in Figure 3. The analysis of the as-deposited state shows that the film exempt of gold exhibited the cubic crystalline structure of YSZ.[13] Small peaks between 53° and 57° originate from the graphite dome used to confine the argon gas near the sample and enable diffraction measurements. A representative length of coherence domains of YSZ of 16 nm has been extracted using the Scherrer formula. The addition of gold to YSZ had a strong impact on the film structure (Figure 3a), as it induced the disappearance of the diffraction signature of the YSZ matrix. We verified by HRTEM that the original structure is retained up to Au/(Au + Zr + Y) = 0.3, as is evidenced on the HRTEM bright-field image (Figure 4) collected on the film with Au/(Au + Zr + Y) = 0.25, where the (200) atomic planes of the YSZ matrix could be identified. Moreover, the elemental map shown in the inset of Figure 4, as well as indexation of the atomic planes as (111) fcc Au in some of the dark regions, confirms the segregation of gold in the oxide matrix at the nanometer scale with an average particle size near 1−2 nm. Above this content, the matrix becomes amorphous, while the signature of crystalline gold could be detected by XRD only for Au/(Au + Zr + Y) above 0.40,[14] but the presence of ultrafine crystalline gold domains (most probable size close to 0.75 nm) was verified using bright- and dark-field TEM analyses, even for the lowest gold content (Supporting Information). Hence, the segregation of crystalline gold is effective for all deposition conditions investigated, despite a deposition temperature close to room temperature.

The XRD diffractograms obtained in the as-deposited state for gold loadings corresponding to the Au/(Au + Zr + Y) ratios of 0.47 and 0.55 (Figure 3a) show the presence of a broad peak at about 44.5°, which was interpreted as the signature of the (111) diffraction peak of fcc gold. Representative lengths of coherence domains of 2 and 6 nm have been extracted using the Scherrer formula for Au/(Au + Zr + Y) = 0.47 and 0.55, respectively. The diffraction profiles have also been collected for similar films annealed for 2 h in air at 400 and 600 °C (Figure 3b,c). The (111) diffraction peak of Au develops and

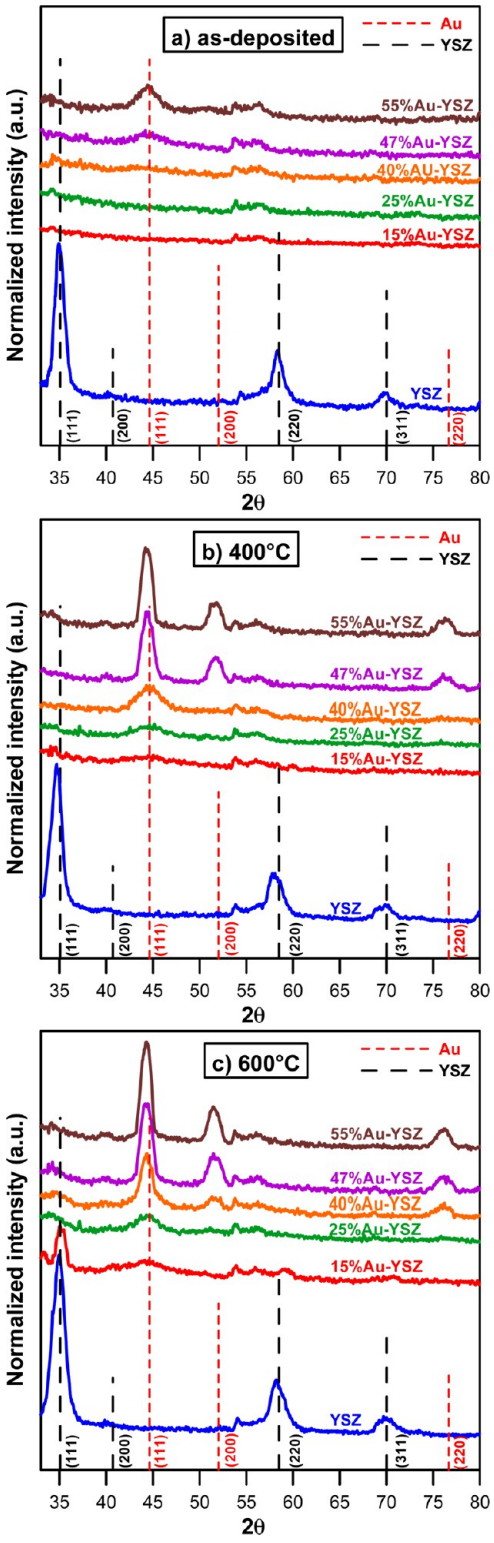

Figure 3. X-ray diffractograms of (a) as-deposited, (b) 400 °C annealed, and (c) 600 °C annealed Au−YSZ thin films.

gets narrower with annealing for all compositions. After annealing Au/(Au + Zr + Y) at 600 °C, we extracted representative lengths of coherence domains of 5, 9, and 12 nm using the Scherrer formula for Au/(Au + Zr + Y) = 0.25, 0.40, and 0.55, respectively. Hence, the annealing treatments were sufficient to trigger the reorganization of gold atoms in the films. It is worth noting that the (200) peak of cubic YSZ

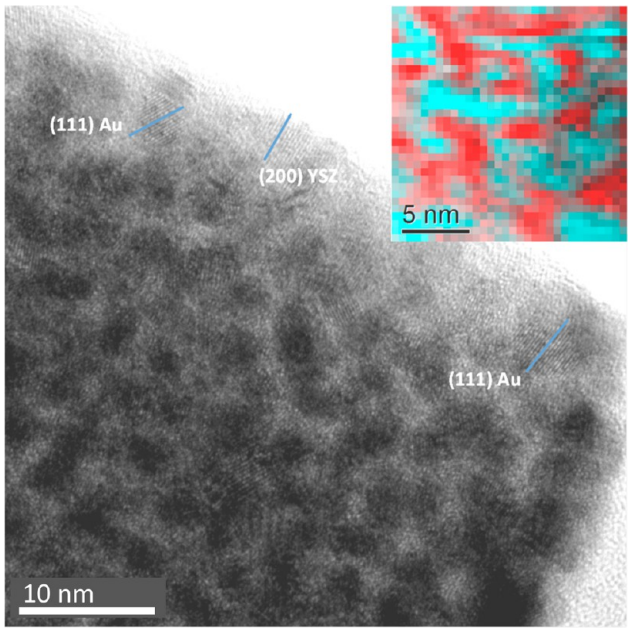

Figure 4. HRTEM bright-field image of the 25% Au−YSZ film. (Inset) Elemental map of (blue) Au and (red) oxygen.

develops after annealing at or above 400 °C for the highest gold loadings of 0.47 and 0.55, which seems contradictory with the degradation of the matrix crystallinity with gold incorporation in as-deposited samples reported above.

To better understand the origin of this observation and to get further information on the film microstructure after annealing, we conducted SEM observations, which are summarized in Figure 5. In Figure 5, panels a and b show the surface morphology of the film with Au/(Au + Zr + Y) = 0.15 annealed in air at 300 and 600 °C, respectively. Significant segregation of gold is observed only for the highest annealing temperature, resulting in the formation of particles in the 10−40 nm range. It also induced the formation of cracks typical for in-plane tensile stresses. The thermal expansion coefficient of silicon and zirconia is close to 4×10^{-6} and 10×10^{-6} K^{-1} in the 25−1000 °C range, respectively, and thus, it can be inferred that for this low gold content, the crack developed during the cooling phase of the annealing treatment. In Figure 5, panels c and d show the surface morphology of the film with Au/(Au + Zr + Y) = 0.25 annealed in air at 300 and 600 °C, respectively. The lowest temperature induced surface segregation of gold in the form of particles with a diameter close to 10 nm. Surprisingly, after annealing at 600 °C, no particle could be found on the film surface at the top of the substrate, but segregation can be observed along the fracture lines at the edge of the silicon substrate cut from a 2 in. wafer before deposition. We do not have an explanation for this behavior. It is worth noting that no cracks have been found by carefully scanning the film surface. Hence, apart from degrading the matrix crystallinity, the incorporation of gold in sufficient amounts strongly modifies the thermomechanical characteristics of the films. The elemental profiles obtained from SIMS measurements (Supporting Information) indicate a rather homogeneous distribution of Au, Zr, and O throughout the film thickness and, overall, minute segregation of gold for Au/(Au + Zr + Y) ratios less than or equal to 0.25, whatever annealing temperature is applied. Therefore, as the coatings keep their

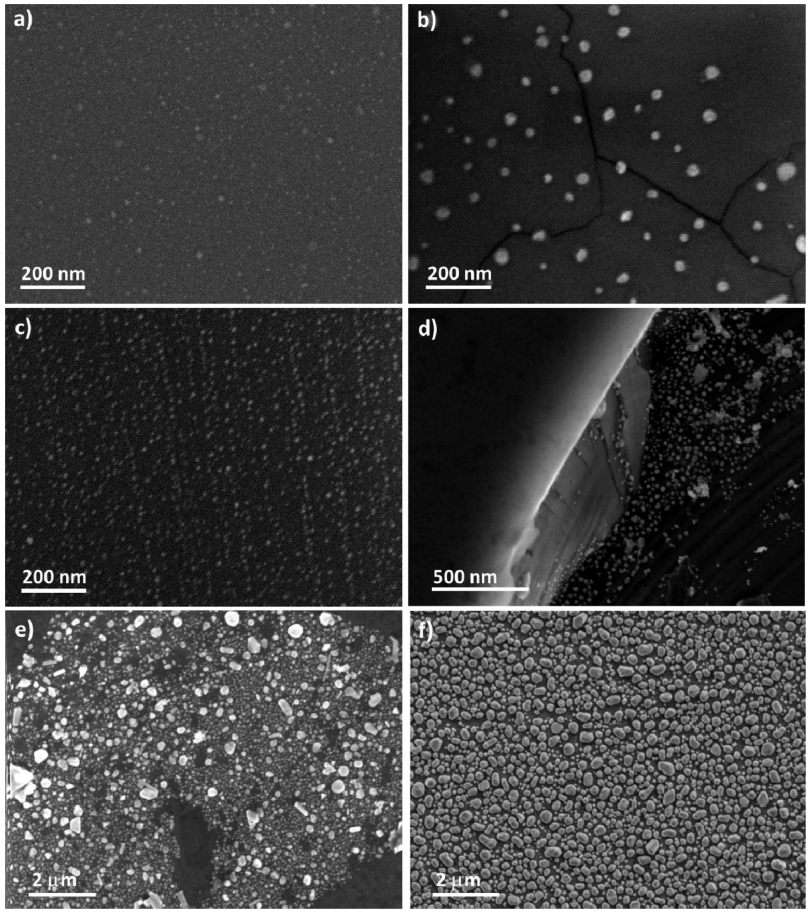

Figure 5. Surface SEM pictures of (a) 15% Au−YSZ and (c) 25% Au−YSZ annealed in air at 300 °C, and (b) 15% Au−YSZ, (d) 25% Au−YSZ, (e) 40% Au−YSZ, and (f) 47% Au−YSZ thin films annealed in air at 600 °C.

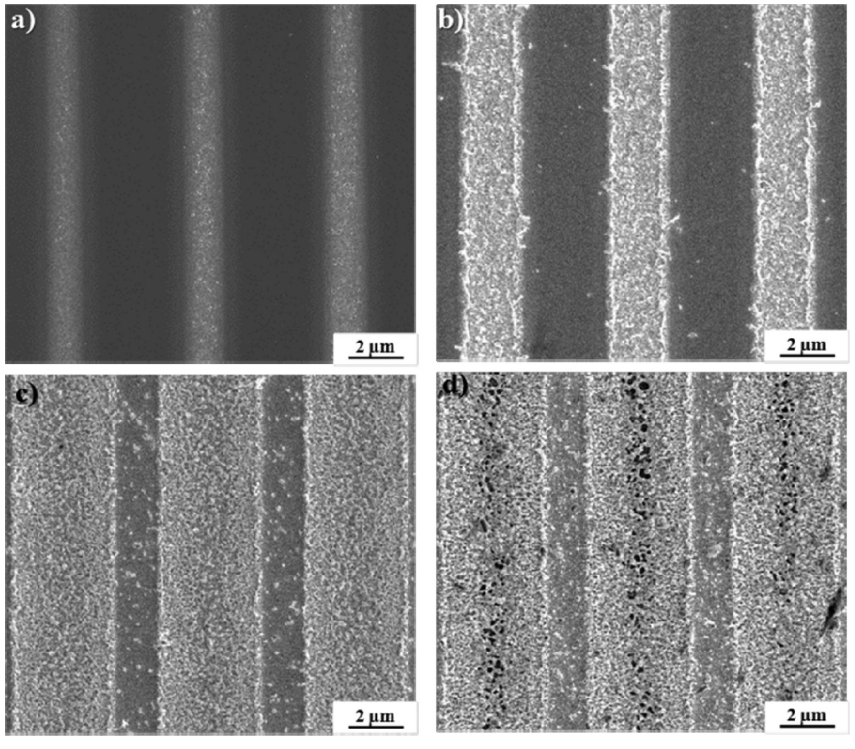

Figure 6. SEM pictures of line patterns with a period close to 5.5 μm produced by the laser interference system at fluences of (a) 45, (b) 91, (c) 145, and (d) 181 mJ/cm^2.

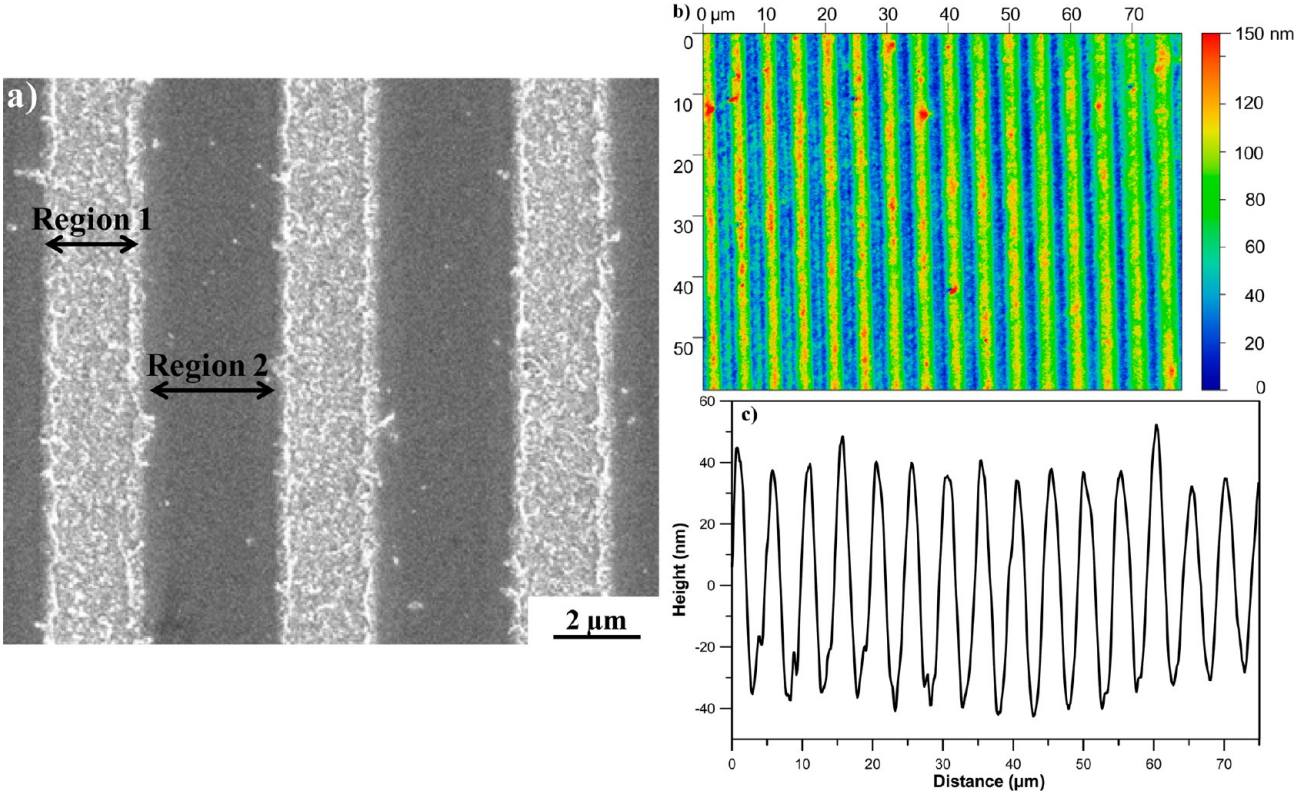

Figure 7. (a) SEM picture of a line pattern with a period close to 5.5 μm produced by the laser interference system at a fluence of 91 mJ/cm^2. Regions 1 and 2 correspond to the laser interference minimum ("untreated") and maximum, respectively. (b) Two-dimensional overview of the laser-treated surface determined using a white light interference (WLI) microscope. (c) Surface profile of patterned 55% Au−YSZ observed perpendicularly to the grid pattern. The positive and negative values correspond to the interference maxima (Region 2) and minima (Region 1), respectively.

integrity, thermal annealing can serve as a platform for a modification of the surface functional properties.

For higher gold loadings, the surface segregation is more marked, as observed in Figure 5, in which panels e and f show the surfaces of films with Au/(Au + Zr + Y) = 0.40 and 0.47, respectively, annealed at 600 °C. A large distribution in the size of gold particles in the 10−500 nm range is obtained for both compositions and for the highest Au/(Au + Zr + Y) ratio of 0.55 (Supporting Information). These sizes are far above the lengths of coherence domains deduced from XRD measurements. This can be explained not only by the presence of smaller particles retained in the YSZ matrix but also by nanoparticles consisting of multiple coherence domains. We performed a further experiment consisting of annealing the same films at 500 °C but deposited on soda-lime glass slides. The surface segregation of gold upon annealing appeared evident only for Au/(Au + Zr + Y) ratios equal to or greater than 0.40, as it changed the sample color from darkish and partly transparent to darkish/yellowish at 0.40 and yellowish for higher gold loadings. Sweeping the film surface with a tissue left apparent only the darkish color for Au/(Au + Zr + Y) = 0.40 and a transparent layer for the two highest loadings. The particles segregated on the top of the films have thereby been removed. From these different observations, it appears that the segregation of gold on the film surface is limited for Au/(Au + Zr + Y) ratios below 0.40 and pronounced for ratios close to 0.40 and above. Taking into account the molar volume of YSZ and gold, the ratios of 0.25 and 0.40 correspond to a volume fraction of gold of 0.21 and 0.33, respectively. Our TEM investigation of the fresh samples with the highest gold loadings tends to indicate that percolation of gold is well established, which may explain these different behaviors.

Figure 6 shows the surface as observed by SEM for films with Au/(Au + Zr + Y) = 0.55 LIP treated with laser fluences of 45, 91, 145, and 181 mJ/cm^2. We found that a certain energy density threshold must be reached in order to produce a homogeneous pattern. Effectively, below laser fluences of 60 mJ/cm^2, modifications of the surface morphology occurred in the regions of interference maxima but with variable amplitude over the spot area. In contrast, fluences lower than 150 mJ/cm^2 are required to avoid ablation damages, melting, and evaporation, as shown in Figure 6d. In this optimal range of laser fluences, a uniform pattern is formed by an alternation of dark and bright parallel lines with different surface morphologies, as shown in Figure 7a. In this figure, Regions 1 and 2 correspond to interference maxima and minima of the LIP process, respectively. A foamy and porous structure is observed in the regions of interference maxima, but Region 2 exhibits a surface morphology that is almost unaffected when compared to the as-deposited film. In Figure 7, panels b and c show the height map obtained by WLI and by surface profile after LIP treatment of this sample, respectively. The laser treatment unambiguously modified the surface morphology and produced a pattern with a height amplitude of about 70 nm. The height shape of the sample perpendicular to the grid pattern presents a sinusoidal form, which is in good agreement with the interference intensity theory.[15] Local modifications of

the microstructure by the LIP will be described in the following section.

To compare the XRD signatures of laser interference patterned and annealed films, GIXRD was carried out on the films with a Au/(Au + Zr + Y) atomic ratio of 0.55 (Figure 7). XRD diffractograms for as-deposited and 600 °C annealed films are also reported. After laser irradiation, the diffractogram exhibits the peaks characteristics of the fcc crystalline structure of gold, but these cannot be correctly fitted using a single Lorentzian function because two contributions are needed (Figure 8 inset). This indicates the presence of two

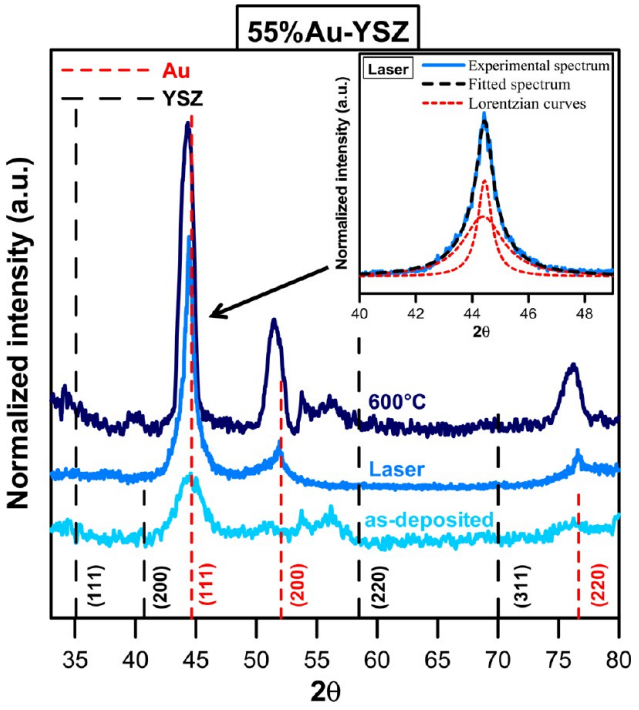

Figure 8. X-ray diffractograms of the as-deposited, 600 °C annealed, and laser interference patterned 55% Au−YSZ. (Inset) Experimental XRD (111) Au peak after laser interference patterning process and the fitted spectrum obtained with two Lorentzian functions.

distributions of crystallites with average sizes of about 5 and 20 nm. It is important to note that the XRD peak broadening by the microstress in thin films is neglected in the Scherrer formula, leading to a tendency to underestimate the grain size. However, the smaller crystallite size is coherent with the value obtained in the corresponding as-deposited film (see section 3.1). To obtain further information on the microstructure of the films in the regions of interference maxima and minima, we conducted TEM investigations on the patterned film.

The bright field corresponding to the region of minimum interference is shown on Figure 8a. Small perturbations of the surface smoothness are observed due to limited displacements and growth of gold particles. The dark spots distributed over the whole film thickness can be attributed to the gold nanoparticles, as gold has the highest atomic mass of the film constituents. The average diameter of the nanoparticles has been estimated to be 6 nm, the same size also extracted from X-ray diffraction analysis on the as-deposited film. Interestingly, this value is also in accordance with the smallest crystallite size contribution obtained from the X-ray diffractogram of the laser treated sample (Figure 8 inset). The corresponding selected area electron diffraction pattern (SAED) shows diffuse diffraction rings, characteristic of nanocrystalline phases (Figure 8b). The rings can be indexed by considering the fcc structures of gold and YSZ.

After laser irradiation, the SAED-pattern (Figure 9d) of the microstructure of the region of maximum interference evidenced a significant growth of gold nanoparticles. Effectively, well-defined diffraction spots ascribed to crystalline gold are observed. As seen in the corresponding bright-field image (Figure 9c), laser irradiation induced crystal growth, which is more pronounced as the film surface is approached. This is associated with a significant increase of the film thickness with amplitude reaching a maximum of 70 nm, consistent with the WLI measurements. The particles can reach diameters greater than 60 nm. A particle size distribution is observed from about 6 to 60 nm above the first 50 nm from the film/substrate interface that appears nearly unaffected by the treatment. As indicated by the XRD analysis discussed above, two distributions of particle sizes are observed. The SAED pattern also shows diffuse diffraction rings, which we attributed to nanocrystalline YSZ. Specifically, we can easily distinguish the (111) ring of YSZ. We have shown elsewhere that this morphology and this microstructure dramatically decrease the friction coefficient.[10] Hereinafter, we investigate the influence of LIP on the electrical resistivity of Au/YSZ films and compare it to the influence of thermal annealing.

3.2. Electrical Properties. The electrical resistivity has been measured in as-deposited, 600 °C annealed, and laser interference patterned films of different contents (Figure 10). For all conditions, the electrical resistivity decreases with the gold content. This result can be explained by an increase in the transfer of electrons between gold particles with gold loading. We ascribe the large decrease in resistivity (approximately 3 orders of magnitude) after thermal annealing in air to the clustering of the gold atoms dispersed in the matrix, growth of pre-existing clusters and precipitates, and surface segregation of films with Au/(Au + Zr + Y) equal or greater than 0.40. Finally, all patterned films have an intermediate resistivity to the as-deposited and 600 °C annealed films, between 1 and 2 orders of magnitude below the resistivity of as-deposited films. Surprisingly, we found only minor differences for the electrical conductivity measured parallel and perpendicular to the interference lines for all compositions explored. This result can only be explained if we consider that diffusion occurred not only in the regions of maximum interference but also in the regions of minimum interference, although very limited modifications of the microstructure could be observed near the surface in the regions of minimum interference (Figure 9a). This hypothesis is supported by the possibility to measure the electrical resistivity for the lowest Au/(Au + Zr + Y) ratio of 0.15, indicating that percolating paths already exist in the as-deposited state. Moreover, the formation of a foamy morphology at the surface of the regions of maximum interference limits the conductivity in this region. The contact potential difference (CPD) between the P-doped silicon tip of an AFM and the surface of the sample of the highest Au/(Au + Zr + Y) ratio of 0.55 treated by LIP is mapped for a selected area including regions of minimum and maximum interference (Figure 11). While the CPD is nearly constant all over the "untreated" region, it fluctuates greatly in the treated region. CPD profiles (Supporting Information) show the CPD is overall higher in the "treated" regions. This reveals that the LIP treatment can modify the work function at the surface of Au−

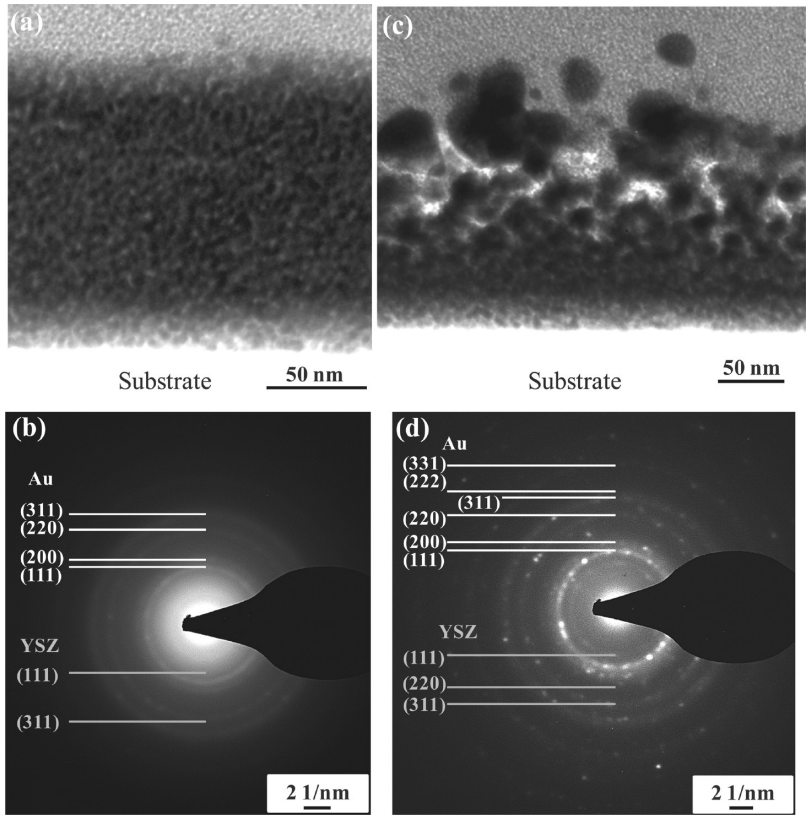

Figure 9. TEM micrographs of the laser interference patterned 55% Au−YSZ thin films. (a and c) Bright-field images in the interference minima (Region 1, Figure 7a) and maxima (Region 2, Figure 7a), respectively. (b and d) Selected area diffraction (SAED) pattern of the Regions 1 and 2, respectively.

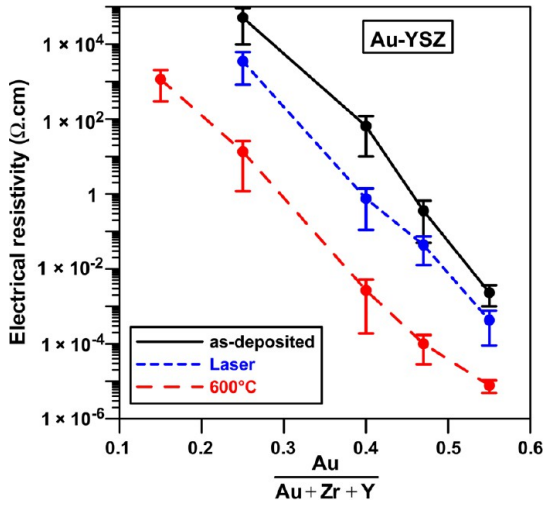

Figure 10. Evolution of electrical resistivity of as-deposited, 600 °C annealed, and laser interference patterned Au−YSZ thin films.

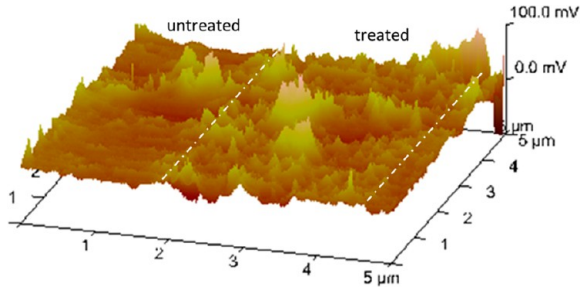

Figure 11. KPFM image of a selected area showing regions of maximum (treated) and minimum (untreated) interference of a laser interference patterned 55% Au−YSZ thin film.

YSZ films and its related properties (catalytic,[16] electronic, etc.).

As a general consideration, the advantage of the LIP treatment over thermal annealing of Au−YSZ nanocomposite films[4,17,18] is the possibility to locally stimulate the relocation of gold but preserve the integrity of the coating for all synthesized compositions. Moreover, the short interaction time (only a few nanoseconds) and limited "heat affected zone" associated with LIP can also be an advantage for particular applications in which only a specific zone, which can be of complex shape, must be treated, or, if that is not possible due to thermal instability of the core material, to heat the whole object or device. This process thereby enables local modification of the electrical resistance of Au−YSZ nanocomposite films in addition to providing improved tribological properties, as already demonstrated.[10] In particular, this finding may be of interest for practical applications in sliding electrical contacts.

4. CONCLUSION

The evolution of the electrical resistivity upon increasing the gold loading, thermal annealing in air, and laser interference patterning (LIP) of thin films consisting of gold nanoparticles embedded in an yttria-stabilized zirconia matrix (Au−YSZ) has been studied using the four-point probe method. The results were explained by evolutions of the microstructure and topography followed by X-ray diffraction, transmission electron

microscopy, and white light interferometry. It was shown that gold segregates in the metallic crystalline state in the YSZ matrix for all synthesis and processing treatments applied, enabling us to lower the electrical resistivity. The advantage of the LIP treatment over conventional thermal annealing is that it enables precise local adjustments of the properties of Au−YSZ thin films and preserves the overall integrity of the films in regard to possible applications such as in the field of catalysis, in active plasmonic devices, and as chemical sensors, to name a few.

■ ASSOCIATED CONTENT

Supporting Information

Microstructure, morphology, and Kelvin probe force microscopy measurements. This material is available free of charge via the Internet at http://pubs.acs.org.

■ AUTHOR INFORMATION

Corresponding Author

*Tel.: +33.383.58.42.52. Fax: +33.383.53.47.64. E-mail: david.horwat@univ-lorraine.fr.

Notes

The authors declare no competing financial interest.

■ ACKNOWLEDGMENTS

The authors acknowledge the German Research Foundation (DFG) for support under project MU 959/20-1 and the BV Matwerk/DFG for the research grant offered for a one-year postdoc for T.G. in Saarbrücken. F.M. and F.S. wish to acknowledge the EFRE funds of the European Commission for support of activities within the AME-Lab project. A.R.L.-C. thanks the Spanish Ministerio de Ciencia e Innovacion for financial support through Project FUNCOAT-CSD2008-00023.

■ REFERENCES

(1) Hutchings, G. J. New Directions in Gold Catalysis. *Gold Bull.* **2004**, *37*, 3−11.
(2) Rogers, P. H.; Carpenter, M. A. Particle Size Sensitivity Dependence of Nanocomposites for Plasmonic-Based All-Optical Sensing Applications. *J. Phys. Chem. C* **2010**, *114*, 11033−11039.
(3) Joy, N. A.; Settens, C. M.; Matyi, R. J.; Carpenter, M. A. Plasmonic Based Kinetic Analysis of Hydrogen Reactions within Au−YSZ Nanocomposites. *J. Phys. Chem. C* **2011**, *115*, 6283−6289.
(4) Voevodin, A. A.; Hu, J. J.; Fitz, T. A.; Zabinski, J. S. Tribological Properties of Adaptative Nanocomposite Coatings Made of Yttria Stabilized Zirconia and Gold. *Surf. Coat. Technol.* **2001**, *146−147*, 351−356.
(5) Mücklich, F.; Lasagni, A.; Daniel, C. Laser Interference Metallurgy—Using Interference as a Tool for Micro/Nano Structuring. *Int. J. Mater. Res.* **2006**, *97*, 1337−1344.
(6) Catrin, R.; Lasagni, A.; Gachot, C.; Schmid, U.; Mücklich, F. Microstructural Design of Advanced Architectures in Titanium/Platinum Thin Films by Laser Interference Metallurgy. *Adv. Eng. Mater.* **2008**, *10*, 466−470.
(7) Gachot, C.; Catrin, R.; Lasagni, A.; Schmid, U.; Mücklich, F. Comparative Study of Grain Size and Orientation in Microstructured Au, Pt, and W Thin Films Designed by Laser Interference Metallurgy. *Appl. Surf. Sci.* **2009**, *255*, 5626−5632.
(8) Catrin, R.; Horwat, D.; Pierson, J. F.; Migot, S.; Hu, Y.; Mücklich, F. Nanoscale and Surface Precipitation of Metallic Particles in Laser Interference Patterned Noble Metal-Based Thin Films. *Appl. Surf. Sci.* **2011**, *257*, 5223−5229.
(9) Lasagni, A.; Holzapfel, C.; Mücklich, F. Periodic Pattern Formation of Intermetallic Phases with Long Range Order by Laser Interference Metallurgy. *Adv. Eng. Mater.* **2005**, *7*, 487−492.
(10) Catrin, R.; Gries, T.; Raillard, B.; Mücklich, F.; Migot, S.; Horwat, D. Influence of Laser Interference Patterning on Microstructure and Friction Behavior of Gold/Yttria-Stabilized Zirconia Nanocomposite Thin Films. *J. Mater. Res.* **2012**, *27*, 879−885.
(11) Klug, H. P.; Alexander, L. E. *X-Ray Diffraction Procedures for Polycrystalline and Amorphous Materials*, 2nd ed.; Wiley-VCH: New York, 1974.
(12) Melitz, W.; Shen, J.; Kummel, A. C.; Lee, S. Kelvin Probe Force Microscopy and Its Application. *Surf. Sci. Rep.* **2011**, *66*, 1−27.
(13) JCPDS − International Centre for Diffraction Data, ICCD Card No. 00-030-1468.
(14) JCPDS − International Centre for Diffraction Data, ICCD Card No. 03-065-2870.
(15) Born, M.; Wolf, E. *Principles of Optics: Electromagnetic Theory of Propagation, Interference and Diffraction of Light*, 7th ed.; Cambridge University Press: Cambridge, U.K., 1999.
(16) Vayenas, C. G.; Bebelis, S.; Ladas, S. Dependence of Catalytic Rates on Catalyst Work Function. *Nature* **1990**, *343*, 625−627.
(17) Hu, J. J.; Voevodin, A. A.; Zabinski, J. S. Application of in Situ Electron Microscopy for Tribological Investigations of Magnetron Sputter Assisted Pulsed Laser Deposition of Yttria-Stabilized Zirconia−Gold Composite Coatings. *J. Mater. Res.* **2005**, *20*, 1860−1868.
(18) Voevodin, A. A.; Hu, J. J.; Jones, J. G.; Fitz, T. A.; Zabinski, J. S. Growth and Structural Characterization of Yttria-Stabilized Zirconia—Gold Nanocomposite Films with Improved Toughness. *Thin Solid Films* **2001**, *401*, 187−195.